1 **Nitrate Chemistry in the Northeast US Part II: Oxygen Isotopes Reveal**

2 **Differences in Particulate and Gas Phase Formation**

3 Heejeong Kim[1,2*], Wendell W. Walters[2*], Claire Bekker[1, a], Lee T. Murray[3], and Meredith G.

4 Hastings[1,2]

5 [1]Department of Earth, Environmental, and Planetary Sciences, Brown University; Providence, RI 02912, USA.

6 [2]Institute at Brown for Environment and Society, Brown University; Providence, RI 02912, USA

7 [3]Department of Earth and Environmental Sciences, University of Rochester; Rochester, NY 14627, USA

8 [a]Now at Environmental Health Sciences, University of California Los Angeles; Los Angeles, CA 90095

9

10 *Correspondence to*:

11 Heejeong Kim (heejeong_kim@brown.edu)

12 Wendell W. Walters (wendell_walters@brown.edu)

13

14 **Abstract.** The northeastern US represents a mostly urban corridor impacted by high population

15 density, high emissions density and degraded air quality and acid rain that has been a focus of

16 regulatory-driven emissions reductions. Detailing the chemistry of atmospheric nitrate formation

17 is critical for improving model representation of atmospheric chemistry and air quality. The

18 oxygen isotope deltas ($\delta(^{18}O)$ and $\Delta(^{17}O)$) of atmospheric nitrate are useful indicators in tracking

19 nitrate formation pathways. Here, we measured $\Delta(^{17}O)$ and $\delta(^{18}O)$ for nitric acid (HNO_3) and

20 particulate nitrate (pNO_3) from three US EPA Clean Air Status and Trends Network (CASTNET)

21 sites in the northeastern US from December 2016 to 2018. The $\Delta(^{17}O, HNO_3)$ and $\delta(^{18}O, HNO_3)$

22 values ranged from 12.9 ‰ to 30.9 ‰ and from 46.9 ‰ to 82.1 ‰, and the $\Delta(^{17}O, pNO_3)$ and

23 $\delta(^{18}O, pNO)$ ranged from 16.6 ‰ to 33.7 ‰ and from 43.6 ‰ to 85.3 ‰, respectively. There was

24 distinct seasonality of $\delta(^{18}O)$ and $\Delta(^{17}O)$ with higher values observed during winter compared to

25 summer, suggesting a shift in O_3 to HO_x radical chemistry, as expected. Unexpectedly, there was

26 a statistical difference in $\Delta(^{17}O)$ between HNO_3 and pNO_3, with higher values observed for pNO_3

27   (27.1±3.8) ‰ relative to HNO_3 (22.7±3.6) ‰, and significant differences in the relationship

28   between $\delta(^{18}O)$ and $\Delta(^{17}O)$. This difference suggests atmospheric nitrate phase-dependent

29   oxidation chemistry that is not predicted in models. Based on output from GEOS-Chem, and both

30   the $\delta(^{18}O)$ and $\Delta(^{17}O)$ observations, we quantify the production pathways of atmospheric nitrate.

31   The model significantly overestimated the heterogeneous N_2O_5 hydrolysis production for both

32   HNO_3 and pNO_3, a finding consistent with observed seasonal changes in $\delta(^{18}O)$, $\Delta(^{17}O)$ and $\delta(^{15}N)$

33   of HNO_3 and pNO_3, though large uncertainties remain in the quantitative transfer of $\delta(^{18}O)$ from

34   major atmospheric oxidants. This comparison provides important insight into the role of oxidation

35   chemistry in reconciling a commonly observed positive bias for model atmospheric nitrate

36   concentrations in the northeastern US.

37

1. Introduction

39   Nitrogen oxides ($NO_x = NO + NO_2$) in the atmosphere have an important impact on air quality and

40   human and ecosystem health (Galloway et al., 2004). NO_x plays an important role in influencing

41   the oxidizing efficiency of the atmosphere, including the production of ozone (O_3), and leads to

42   the formation of atmospheric nitrate (gas phase nitric acid (HNO_3) and nitrate in particulate form

43   (pNO_3)) (Crutzen et al., 1979). HNO_3 and pNO_3 are, in turn, important contributors to dry and wet

44   N deposition. Nitrate is a key component of particulate matter ($PM_{2.5}$), which has direct adverse

45   effects on human respiratory and climate change, and the deposition of N to ecosystems can

46   contribute to soil acidification and eutrophication (Camargo and Alonso, 2006; Schlesinger, 2007;

47   Tai et al., 2010). Thus, changes in the chemistry and chemical feedbacks associated with NO_x have

48   important implications for predicting air quality improvements and climatic responses.

49

50   The US Environmental Protection Agency (EPA) reported that NO_x emissions have decreased by

51   36 % in the United States from 2007 to 2015 due to effective regulations in response to the Clean

52   Air Act and its Amendments (US EPA, 2017; CASTNET, 2019; NEI, 2017; Shah et al., 2018).

53   However, atmospheric pNO_3 concentrations have responded sub-linearly to the dramatic NO_x

54   emission reductions with only a 7.8 % pNO_3 decrease over the same period in the northeastern US.

55   Uncertainties in our understanding between NO_x reductions and the production of atmospheric

56   nitrate challenge our ability to make effective reductions in reactive nitrogen concentrations. Major

57   factors influencing atmospheric nitrate production include oxidant availability, heterogeneous

58   chemistry, gas-to-particle partitioning, and potential aerosol nitrate photolysis (Jaeglé et al., 2018;

59   Shah et al., 2018; Kasibhatla et al., 2018).

60

61   Atmospheric nitrate concentrations have been simulated using various chemistry models to detail

62   spatiotemporal variabilities between precursor NO_x emissions and nitrate in the US, with

63   somewhat limited success (Walker et al., 2012; Zhang et al., 2012). In particular, the

64   concentrations of nitrate observed in the northeastern US tend to be overestimated in models (e.g.,

65   Heald et al., 2012; Zhang et al., 2012), which is an important region to monitor due to its high

66   population density, transport patterns and the tendency for poor air quality (Sickles and Shadwick,

67   2015). Modeling studies suggest that biases revealed by comparison with observations are likely

68   due to uncertainties in NO_x and NH_3 emission estimates, dry deposition removal rates,

69   heterogeneous chemical production rates, and changing chemistry due to reductions in NO_x and

70   sulfur dioxide emissions (Heald et al., 2012; Holt et al., 2015; Shah et al., 2018).

71

72   The nitrate oxygen isotope deltas ($\Delta(^{17}O)$ and $\delta(^{18}O)$) has proven to provide observational

73   constraints on the oxidation pathways that are responsible for the formation of atmospheric nitrate

74   (Hastings et al., 2003; Michalski et al., 2003; Alexander et al., 2009). The isotopic composition is

75   expressed as δ, which is a standardized notation and quantified as $\delta = (R_{sample}/R_{reference} - 1)$. R is

76   the ratio of the heavy isotope to the light isotope (e.g., $^{18}O/^{16}O$; $^{17}O/^{16}O$) in the sample and

77   internationally recognized isotopic reference material (Oxygen = Vienna Standard Mean Ocean

78   Water), respectively. Several studies have suggested that the distinctive ($\Delta(^{17}O) = \delta(^{17}O) - 0.52 \times$

79    $\delta(^{18}O)$) and $\delta(^{18}O)$ signatures of atmospheric oxidants such as O_3, $O_2/RO_2/HO_2$, H_2O and OH are

80   incorporated into nitrate, tracking the oxidation chemistry of NO_x (Hastings et al., 2003; Michalski

81   et al., 2003; Savarino et al., 2007). Traditionally, the influence of O_3 incorporation in nitrate has

82   been quantitively tracked using only $\Delta(^{17}O)$, because of the unique mass independent fractionation

83   that results in O_3 carrying excess $\delta(^{17}O)$ yielding a transferrable $\Delta(^{17}O) = (39\pm2)$ ‰ (Thiemens,

84   2006; Vicars and Savarino, 2014). However, all other atmospheric oxidants contain expected mass

85   dependent signatures such that all have $\Delta(^{17}O)$ value of approximately 0 ‰. The $\delta(^{18}O)$ of

86   atmospheric oxidants could provide further insights into nitrate production mechanisms, especially

87   in cases where oxidants other than O_3 are important, since it is distinctive for each oxidant (e.g.,

Atmospheric
Chemistry
and Physics
Discussions

Open Access

EGU

88 $\delta(^{18}O, O_3) = (126.3 \pm 12)$ ‰, $\delta(^{18}O, O_2) = 23$ ‰, $\delta(^{18}O, OH) = -43$ ‰ (Michalski et al., 2012; Vicars

89 and Savarino, 2014)).

90

91 Using the Clean Air Status and Trends Network (CASTNET) samples, we explore spatiotemporal

92 differences in HNO_3 and pNO_3 concentrations and production mechanisms in the northeastern US.

93 The observations reveal unique oxidant relationships ($\Delta(^{17}O)$ vs. $\delta(^{18}O)$) for HNO_3 versus pNO_3,

94 which are not predicted in atmospheric chemistry models. Using output from a state-of-the-art

95 atmospheric chemistry model (GEOS-Chem) we find that the model well predicts the seasonality

96 of observed $\Delta(^{17}O)$ values, despite significant overestimation of HNO_3 and pNO_3 concentrations.

97 However, a comparison with the combination of $\Delta(^{17}O)$ and $\delta(^{18}O)$ values of HNO_3 and pNO_3

98 clearly identify weaknesses in our understanding of the importance of different chemical

99 production mechanisms.

100

2. Methods

2.1 CASTNET

103 Atmospheric nitrate samples were collected by the US EPA at several locations of Clean Air Status

104 and Trends Network (CASTNET) sites in the northeastern US (**Figure 1**). Three CASTNET sites

105 were selected: Abington, CT (ABT147, 41.84° N, -72.01° W), Connecticut Hill, NY (CTH110,

106 42.40° N, -76.65° W), Woodstock, NH (WST109, 43.94° N, -71.70° W). The samples were

107 collected weekly from December 23, 2016, to December 28, 2018, using a three-stage filter pack

108 system. Based on EPA protocols, pNO_3 was collected using a Teflon filter in the first stage of the

109 filter pack, and gaseous HNO_3 was collected using a Nylon filter in the second stage of the filter

110 pack. We note that due to the semi-volatile characteristic of ammonium nitrate, some pNO_3 might

111 volatilize as HNO_3 and collect downstream of the filter pack leading to negative biases for pNO_3

112 and positive biases for HNO_3 collection (Hering and Cass, 1999; Ashbaugh and Eldred, 2004).

113

2.2 Concentration and Isotope Analysis

115 Filters were extracted and measured for nitrate concentration using Ion Chromatography and then

116 stored in the CASTNET laboratory at room temperature for up to two years. Extracted samples

117 were shipped to Brown University in summer 2020. Nitrate concentrations were measured at

118 Brown University to check for stability of NO_3^- using standard colorimetric methods (i.e., US EPA

119   Method 353.2) on an automated discrete UV-Vis Analyzer (SmartChem Westco Scientific

120   Instruments, Inc.). The limit of detection was 0.1 and 0.3 μM for NO_2^- and NO_3^-, respectively, and

121   the pooled standard deviation of replicate quality control standards was better than 3 %. Overall,

122   strong positive correlations were found between measured concentrations at Brown and reported

123   CASTNET data for both HNO_3 ($y = 0.99x – 0.08$ ($R^2 = 0.99$); $p < 0.05$) and pNO_3 ($y = 1.04x +$

124   0.09 ($R^2 = 0.99$); $p < 0.05$) (**Figure 2**); we therefore consider the samples representative of their

125   original concentrations.

126

127   The samples were collected once a week, and equal volumes of filter extract were combined for

128   isotope analysis to produce monthly aggregates for HNO_3 and pNO_3, respectively. Oxygen ($\delta(^{18}O)$

129   and $\Delta(^{17}O)$) stable isotopic compositions in HNO_3 and pNO_3 were analyzed utilizing the bacterial

130   denitrifier method at Brown University (Sigman et al., 2001; Casciotti et al., 2002; Kaiser et al.,

131   2007). Briefly, samples were injected into a buffer solution containing *P. aureofaciens,* which lack

132   the nitrous oxide (N_2O) reductase enzyme, and sample NO_3^- is quantitatively reduced to N_2O. For

133    $\delta(^{18}O)$ analysis, the generated N_2O is injected into a Thermo-Finnegan Delta V Plus isotope ratio

134   mass spectrometry (IRMS) with a modified Gas Bench system after flowing through an automated

135   extraction and purification system. Determination of $\delta(^{18}O)$ in N_2O was conducted at an *m/z* of 44,

136   45, and 46 and corrected using internationally recognized isotopic reference materials that included

137   IAEA-NO_3 (25.6 ‰), USGS34 (-27.9 ‰), and USGS35 (57.5 ‰). The $\Delta(^{17}O)$ was determined in

138   a separate analysis. The bacteria-generated N_2O was decomposed to N_2 and O_2 in a gold furnace

139   heated to 770 ºC and analyzed at *m/z* 32, 33, and 34 to determine $^{17}O/^{16}O$ and $^{18}O/^{16}O$ ratios of the

140   evolved O_2. The 33/32 and 34/32 mass ratios were corrected using isotopic reference materials,

141   USGS34 (-0.29 ‰) and USGS35 (21.6 ‰), and then $\Delta(^{17}O)$ is determined from $\Delta(^{17}O) = \delta(^{17}O) -$

142    $0.52 \times \delta(^{18}O)$. Due to sample mass limitations, some samples were only analyzed for $\delta(^{18}O)$. The

143   number of samples that were not measured for $\Delta(^{17}O)$ was 1 HNO_3 sample from CTH110, 2 HNO_3

144   samples from ABT147, 5 pNO_3 samples from CTH110, and 16 pNO_3 samples from WST109. The

145   overall pooled standard deviations of isotopic reference materials and sample numbers were as

146   followed: USGS34 ($\sigma(\delta(^{18}O)) = 0.5$ ‰ ($n = 21$); $\sigma(\Delta(^{17}O)) = 1.1$ ‰ ($n = 26$)); USGS35 ($\sigma(\delta(^{18}O))$

147    $= 0.4$ ‰ ($n = 27$); $\sigma(\Delta(^{17}O)) = 2.4$ ‰ ($n = 26$)), and IAEA-N3 ($\sigma(\delta(^{18}O)) = 0.3$ ‰ ($n = 23$)).

148

149   **2.3 GEOS-Chem**

Atmospheric
Chemistry
and Physics
Discussions

150 The GEOS-Chem global model of atmospheric chemistry (www.geos-chem.org) was utilized to

151 track the production of NO_2 and HNO_3 at the CASTNET sites to model $\delta(^{18}O)$ and $\Delta(^{17}O)$ isotope

152 following previous framework (Alexander et al., 2020). We use version 13.2.1

153 (doi:10.5281/zenodo.5500717) of the model driven by GEOS5-FP assimilated meteorology from

154 the NASA Global Modeling and Assimilation Office (GMAO). A nested grid (0.25° latitude ×

155 0.3125° longitude horizontal resolution; ~25 km) simulation was conducted over the northeastern

156 United States (97°-60° W; 35°-60° N) in 2017 and 2018. Boundary conditions were from global

157 simulations performed at 4° latitude × 5° longitude horizontal resolution for the same years after

158 a one-year initialization. Gas- and aerosol-phase chemistry was simulated using the default

159 "fullchem" mechanism (Bates and Jacob, 2019; Wang et al., 2021). Inorganic gas and aerosol

160 partitioning were conducted using version 2.2 of the ISORROPIA II thermodynamic equilibrium

161 model (Fountoukis and Nenes, 2007). All default anthropogenic emissions were applied, which is

162 primarily version 2.0 of the Community Emissions Data System (Hoesly et al., 2018) as

163 implemented by McDuffie et al. (2020). Natural emissions respond to local meteorology and

164 include biogenic VOCs from terrestrial plants and the ocean (Millet et al., 2010; Guenther et al.,

165 2012; Hu et al., 2015; Breider et al., 2017), NO_x from lightning and soil microbial activity (Murray

166 et al., 2012; Hudman et al., 2012), mineral dust (Ridley et al., 2012), and sea salt (Jaeglé et al.,

167 2011; Huang and Jaeglé, 2017). Biomass burning emissions were monthly means from version

168 4.1s of the Global Fire Emissions Database (GFED4.1s; van der Werf et al., 2017). Wet deposition

169 for water-soluble aerosols is described by Liu et al. (2001) and by Amos et al. (2012) for gases.

170 Dry deposition is based on the resistance-in-series scheme of Wesely (1989). Diagnostics were

171 implemented to archive the total production and loss pathways of NO_y, NO_x, NO_2, $RONO_2$, HNO_3

172 and pNO_3, including the net flux of mass between HNO_3 and pNO_3 in ISOROPPIA II. Model skill

173 was assessed with the Normalized Mean Bias (B) metric, defined as $B = (\sum (\bar{Q}_m - \bar{Q}_o) / \sum \bar{Q}_o)$

174 where $\bar{Q}_m$ = modeled quantities and $\bar{Q}_o$ = observed quantities.

175

176 **2.4 $\delta(^{18}O)$ and $\Delta(^{17}O)$ calculations**

177 The oxygen isotope compositions ($\delta(^{18}O)$ and $\Delta(^{17}O)$) of nitrate were calculated based on oxygen

178 isotope mass-balance using production rate outputs from the GEOS-Chem global 3-D model and

179 compared with our observations. Expected $\delta(^{18}O)$ and $\Delta(^{17}O)$ ranges resulting from nitrate

180 production pathways have been previously described and calculated using oxygen mass-balance

181   (Alexander et al., 2009, 2020; Michalski et al., 2003; Morin et al., 2011; Carter et al., 2021). Briefly,

182   the $\delta(^{18}O)$ and $\Delta(^{17}O)$ of nitrate are determined by both NO_x photochemical cycling and nitrate

183   formation reactions (Alexander et al., 2009; Walters et al., 2018). During NO_x photochemical

184   cycling, the oxygen isotopic compositions of NO_x is determined by the relative production rates of

185   NO_2 via reaction of NO with O_3, peroxy and hydroperoxyl radicals, and halogen oxides (XO; BrO,

186   ClO). The proportional contribution of O_3 during NO oxidation is denoted as A and is calculated

187   using

188

189    $A = (k(O_3+NO)\ [O_3] + k(XO+NO)[XO])/(k(O_3+NO)[O_3] + k(XO+NO)[XO] + k(HO_2+NO)[HO_2]$

190    $+ k(RO_2+NO)[RO_2])$ (Eq. 1)

191

192   where k is the respective rate constant for NO oxidation via O_3, XO, HO_2, and RO_2. The $\Delta(^{17}O)$

193   value of the terminal oxygen atom in $O_3(O_3^*)$ is assumed to be (39 ± 2) ‰ based on observations,

194   while all other oxidants are assumed to be 0 ‰ (Vicars et al., 2012; Vicars and Savarino, 2014;

195   Alexander et al., 2020). $\delta(^{18}O)$ and $\Delta(^{17}O)$ values of nitrate from each production pathway were

196   then determined using O mass-balance based on the O transfer from varying oxidants involved in

197   its formation (**Table 1**).

198

199   The GEOS-Chem global model has been previously used to quantify nitrate production pathways

200   based on $\Delta(^{17}O)$ (Alexander et al., 2009, 2020), but this has not been done for $\delta(^{18}O)$. Using a

201   similar framework as for $\Delta(^{17}O)$, we expect that $\delta(^{18}O)$ of NO_2 reflects isotopic signatures of both

202   O_3 and O_2, as it has been assumed that the O isotopic composition of RO_2 and HO_2 is equal to O_2

203   (Michalski et al, 2012; Walters et al., 2018). Accordingly, the values of $\delta(^{18}O, NO_2)$ can be

204   predicted by the proportional contribution of O_3 and both HO_2 and RO_2 during NO_x cycling with

205   their distinct $\delta(^{18}O)$ values of O_3 and O_2 (Eq. 2; **Table 1**).

206

207    $\delta(^{18}O, NO_2) = A(\delta(^{18}O, O_3^*)) + (1-A)(\delta(^{18}O, O_2))$ (Eq.2)

208

209   The $\delta(^{18}O)$ values of O_3 and O_2 are adopted from previous studies that determined $\delta(^{18}O, O_3^*)$ and

210    $\delta(^{18}O, O_2)$ as 126.3 ‰ and 23 ‰ (Vicars and Savarino, 2014; Kroopnick and Craig, 1972,

211   respectively). For the calculation of $\delta(^{18}O)$ of nitrate, the value of $\delta(^{18}O)$ of $H_2O(l)$ is assumed to

212   be -6 ‰, which is a typical mid-latitude value and represents water in the liquid phase incorporated

213   into nitrate formation associated with heterogeneous reactions by N_2O_5 or NO_2 hydrolysis

214   (Michalski et al, 2012). The $\delta(^{18}O)$ value of OH can be dependent on both O_3 and $H_2O(g)$, as well

215   as environmental conditions since oxygen in OH can exchange with $H_2O(g)$ (Dubey et al. 1997).

216   Fractionation factors associated with the O transfer into NO_y products are unknown and therefore

217   were not considered. The $\delta(^{18}O)$ of $H_2O(g)$ was estimated based on the equilibrium between $H_2O(l)$

218   and $H_2O(g)$ with a temperature-dependent fractionation factor (1.0094 at 298K); it is assumed that

219   OH and $H_2O(g)$ exist in isotopic equilibrium, which has a theoretically determined fractionation

220   factor (1.0371 at 298K) and leads to an estimate of $\delta(^{18}O, OH)$ of -43 ‰ (Michalski et al, 2012;

221   Walters and Michalski, 2016). We note that the typical annual temperature for the northeast US is

222   approximately 287 K, yielding a $\delta(^{18}O, OH)$ of -45 ‰; for comparison purposes with prior

223   publications, we utilize -43 ‰, which makes little difference in the quantitative results below. In

224   the final step, $\delta(^{18}O)$ or $\Delta(^{17}O)$ of total atmospheric nitrate were calculated based on the monthly-

225   averaged production rates from GEOS-Chem and the seven major reactions that produce nitrate in

226   the model (**Table 1**) to compare with observations.

227

228

229   **3. Results and discussions**

230   **3.1 Spatiotemporal variations of atmospheric nitrate concentration**

231

232   **Figure 3** shows the monthly averaged spatiotemporal variations of HNO_3 and pNO_3 mass

233   concentration (denoted as γ). The observed HNO_3 concentrations ($\gamma_o(HNO_3)$) ranged from 0.11 µg

234   m^{-3} to 0.88 µg m^{-3}, with a mean value of 0.46 µg m^{-3} across the three CASTNET sites. The

235   observed pNO_3 concentrations ($\gamma_o(pNO_3)$) ranged from 0.04 µg m^{-3} to 2.01 µg m^{-3}, with a mean

236   value of 0.50 µg m^{-3}, and showed clear seasonality at all three sites with averaged higher values

237   (0.75±0.52) µg m^{-3} in the cold season (October to March) and lower values (0.25±0.17) µg m^{-3} in

238   the warm season (April to September), which were significantly different ($p < 0.01$). On the other

239   hand, $\gamma_o(HNO_3)$ was seasonally invariable with (0.42±0.17) µg m^{-3} for cold season and (0.50±0.24)

240   µg m^{-3} for warm season that was not statistically different ($p > 0.05$). Averaged $\gamma_o(HNO_3)$ was

241   generally lower than pNO_3 across the sites, but the difference was statistically insignificant ($p >$

242   0.05). Both $\gamma_o(HNO_3)$ and $\gamma_o(pNO_3)$ indicated spatial variability with higher values at ABT147 and

243   CTH110 than the WST109 site. The mean annual $\gamma_o(HNO_3)$ and $\gamma_o(pNO_3)$ were (0.61 ± 0.15) µg m^{-3}

244   and (0.66 ± 0.34) µg m^{-3} at ABT147, (0.55 ± 0.13) µg m^{-3} and (0.68 ± 0.58) µg m^{-3} at CTH110, and

245   (0.22 ± 0.06) µg m^{-3} and (0.17 ± 0.13) µg m^{-3} at WST109, respectively.

246

247   The modeled HNO$_3$ concentrations ($\gamma_m(HNO_3)$) ranged from 0.20 µg m^{-3} to 2.36 µg m^{-3}, with a

248   mean value of 0.82 µg m^{-3} and modeled pNO$_3$ concentrations ($\gamma_m(pNO_3)$) ranged from 0.20 µg m^{-3}

249   to 5.27 µg m^{-3}, with a mean value of 1.89 µg m^{-3}. Contrary to our observed data, no consistent

250   spatial variability was observed for $\gamma_m(HNO_3)$ and $\gamma_m(pNO_3)$. The mean $\gamma_m(HNO_3)$ and $\gamma_m(pNO_3)$

251   were (1.09 ± 0.62) µg m^{-3} and (1.73 ± 1.13) µg m^{-3} at ABT147, (0.74 ± 0.46) µg m^{-3} and (2.42 ± 1.71)

252   µg m^{-3} at CTH110, and (0.64 ± 0.22) µg m^{-3} and (1.52 ± 1.24) µg m^{-3} at WST109, respectively.

253   Overall, simulated atmospheric nitrate in the GEOS-Chem model is significantly overestimated

254   across the three CASTNET sites: $\gamma_m(HNO_3)$ are 2-3 times higher than the $\gamma_o(HNO_3)$ and $\gamma_m(pNO_3)$

255   are 3-9 times higher than $\gamma_o(pNO_3)$.

256

257   As stated above, there can be negative biases for pNO$_3$ and positive biases for HNO$_3$ collection,

258   but these should be reduced by comparing the model to total atmospheric nitrate (tNO$_3$ = HNO$_3$ +

259   pNO$_3$). Still, the simulated tNO$_3$ concentration ($\gamma_m(tNO_3)$) with GEOS-Chem is significantly

260   overestimated relative to observations ($\gamma_o(tNO_3)$; B = 182 %; **Figure 3**). While the simulated pNO$_3$

261   well reproduces the observed seasonality (high concentrations in the cold season and vice versa),

262   it highly overestimated the concentrations for most of the year (B = 276 %; **Figure 3**). The

263   simulated HNO$_3$ did not capture the observed relative lack of seasonality, instead showing clear

264   seasonality with generally high concentrations in the warm season and low in the cold season. The

265   lack of agreement between GEOS-Chem and nitrate observations is consistent with previously

266   reported results in other studies (Heald et al., 2012; Zhang et al., 2012; Walker et al., 2012).

267   Uncertainties in N$_2$O$_5$ hydrolysis rate, emission estimates, or dry and wet deposition removal rates

268   have been suggested as possible causes for predicted nitrate biases. For instance, Luo et al., 2019;

269   2020 reported dramatic improvement of nitric acid and nitrate biases by updating wet scavenging

270   parameterization in the GEOS-Chem model; however, this update leads to biases in oxidized

271   nitrogen wet deposition between model predictions and observations.

272

273 **3.2 Oxygen isotopic compositions ($\delta(^{18}O)$ and $\Delta(^{17}O)$) – Oxidation Chemistry and Phase**

274 **Difference**

275

276 The oxygen isotopic compositions in atmospheric nitrate are used to evaluate NO_x oxidation

277 chemistry and to assess seasonal changes in nitrate formation mechanisms. For the CASTNET

278 sites, the $\Delta(^{17}O, HNO_3)$ and $\Delta(^{17}O, pNO_3)$ values ranged from 12.9 ‰ to 30.9 ‰ and from 16.6 ‰

279 to 33.7 ‰, with a mean value of (22.7 ± 3.6) ‰ and (27.1± 3.8) ‰, respectively (**Figure 4a and**

280 **b**). The $\delta(^{18}O, HNO_3)$ and $\delta(^{18}O, pNO_3)$ values ranged from 46.9 ‰ to 82.1 ‰ and from 43.6 ‰

281 to 85.3 ‰, with a mean value of (68.1 ± 7.1) ‰ and (68.2 ± 8.3) ‰, respectively (**Figure 4c and**

282 **d**). These observations are in the range of previously reported values in polluted mid-latitudes:

283 $\delta(^{18}O, HNO_3)$ and $\delta(^{18}O, pNO_3)$ in CASTNET sites in Ohio, Pennsylvania, and New York from

284 April 2004 to March 2005 ranged from 51.6 ‰ to 94.0 ‰ and from 45.2 ‰ to 92.7 ‰ (Elliott et

285 al., 2009), respectively. They are also consistent with observations of polluted air masses in

286 Canada from September 2010 to January 2014 were from 62.4 to 81.7 ‰ for $\delta(^{18}O, HNO_3)$, from

287 19.3 to 29.0 ‰ for $\Delta(^{17}O, HNO_3)$, from 48.4 to 83.2 ‰for $\delta(^{18}O, pNO_3)$, and from 13.8 to 30.5 ‰

288 for $\Delta(^{17}O, pNO_3)$ (Savard et al., 2018).

289

290 Previous studies and modeling results have indicated that the seasonality of oxygen isotopic

291 compositions in HNO_3 and pNO_3 is driven by a shift in oxidation chemistry (Hastings et al., 2003;

292 Michalski et al, 2012; Alexander et al., 2009; 2020). Globally, the seasonality reflects a shift in O_3

293 to HO_x radical chemistry during winter to summer, respectively. Wintertime has higher $NO + O_3$

294 branching ratios than summer, which has increased $NO + RO_2/HO_2$. The high values of $\delta(^{18}O)$ and

295 $\Delta(^{17}O)$ in HNO_3 and pNO_3 during the cold season are caused by the increased incorporation of O_3

296 into the nitrate product through N_2O_5 heterogeneous hydrolysis on aerosols. In contrast, the

297 dominance of gas-phase production by the $NO_2 + OH$ reaction dilutes the isotopic influence of O_3

298 during warm seasons leading to the low values of $\delta(^{18}O)$ and $\Delta(^{17}O)$ in HNO_3 and pNO_3 (**Figure**

299 **4**). Spatial variability is observed in $\delta(^{18}O)$ and $\Delta(^{17}O)$ of HNO_3, with highest values at CTH110

300 ($\delta(^{18}O)$: (71.5±5.6) ‰ ($n = 24$) and $\Delta(^{17}O)$: (25.0±3.1) ‰ ($n = 23$)) followed by ABT147 ($\delta(^{18}O)$:

301 (70.1±4.8) ‰ ($n = 24$) and $\Delta(^{17}O)$: (23.1±2.2) ‰ ($n = 24$)) and WST109 ($\delta(^{18}O)$: (62.8±7.7) ‰ (n

302 $= 24$) and $\Delta(^{17}O)$: (20.2±3.7) ‰ ($n = 24$)). However, $\delta(^{18}O)$ and $\Delta(^{17}O)$ of pNO_3 were not

303 significantly different across the stations: for ABT147 ($\delta(^{18}O)$: (68.6±7.1) ‰ ($n = 24$) and $\Delta(^{17}O)$:

304   (26.4±3.6) ‰ (n = 22)); CTH110 ($\delta(^{18}O)$: (69.1±8.9) ‰ (n = 24) and $\Delta(^{17}O)$: (26.8±4.1) ‰ (n =

305   19)); and WST109 ($\delta(^{18}O)$: (66.8±8.7) ‰ (n = 24) and $\Delta(^{17}O)$: (29.4±2.9) ‰ (n = 10)).

306

307   Our observations indicate a significant phase-dependent difference in oxidation chemistry between

308   HNO_3 and pNO_3 that is unexpected. Many modeled mechanisms of gas- and aqueous-phase

309   chemistry produce HNO_3, then HNO_3 is partitioned into the aerosol phase based on

310   thermodynamic equilibrium (i.e., $NH_4NO_3(s) \rightleftharpoons HNO_3(g) + NH_3(g)$) or coarse uptake.

311   Conventional understanding would expect $\Delta(^{17}O)$ of HNO_3 and pNO_3 to be the same (e.g.,

312   Alexander., 2020). However, observed $\Delta(^{17}O, pNO_3)$ tends to be significantly higher than $\Delta(^{17}O,$

313     $HNO_3)$ ($p < 0.01$ at ABT and CTH, $p = 0.088$ at WST). This phase difference in $\Delta(^{17}O)$ cannot be

314   explained by potential sample biases caused by volatilization, which leads to mass-dependent

315   fractionation. This difference might be related to the differences in particulate nitrate size-

316   dependent production pathways. Previous studies of size-segregated $\Delta(^{17}O, pNO_3)$ indicated

317   higher values for coarse pNO_3 (aerodynamic diameter (D_a) > 0.95 μm) relative to fine pNO_3 (D_a

318   < 0.95 μm) that was concluded to reflect the increased importance of heterogeneous N_2O_5

319   hydrolysis on coarse particles relative to fine particles (Vicars et al., 2013). The CASTNET pNO_3

320   samples reflect total suspended particles (TSP) such that increased importance of N_2O_5

321   heterogeneous chemistry for coarse particulate nitrate formation could explain the higher $\Delta(^{17}O,$

322     $pNO_3)$ values we observe relative to $\Delta(^{17}O, HNO_3)$.

323

324   We also observed different $\delta(^{18}O)$ and $\Delta(^{17}O)$ relationships for HNO_3 and pNO_3, which further

325   suggests phase-dependent nitrate oxidant chemistry. Positive linear relationships between $\delta(^{18}O)$

326   and $\Delta(^{17}O)$ were observed for HNO_3 and pNO_3 across the CASTNET sites, with similar slopes but

327   different oxygen isotopic signatures indicated by different intercepts (**Figure 5**). For the

328   relationship of $\delta(^{18}O)$ and $\Delta(^{17}O)$, the high end-member should result from O_3 and the lower end-

329   member depends on the isotopic signature of the atmospheric oxidants involved. The transferable

330     $\delta(^{18}O)$ signatures of atmospheric oxidants are not fully understood yet, reflecting a complex

331   combination of atmospheric oxidant source signatures and isotope fractionation during reaction

332   and incorporation into the nitrate end-product. While ozone has a notable high $\Delta(^{17}O)$ value ((39±2)

333   ‰; Vicars and Savarino, 2014), $\Delta(^{17}O)$ values of other atmospheric oxidants such as $O_2/RO_2/HO_2$,

334   H_2O and OH are equal to or close to 0 ‰ (Michalski et al., 2012; Walters et al., 2019). Overall,

11

335   our results suggest more O_3 is incorporated during the formation of pNO_3 than HNO_3. We further

336   analyze the oxidation chemistry involved in atmospheric nitrate formation based on output from

337   the GEOS-Chem chemical transport model.

338

339   **3.3 Quantifying oxidation chemistry in atmospheric nitrate production mechanisms**

340   Observations of the oxygen isotopic composition were utilized to quantify the relative importance

341   of different nitrate formation pathways and to assess model representation of the chemistry of

342   nitrate formation. Using atmospheric nitrate production rates from the GEOS-Chem model, $\Delta(^{17}O)$

343   was calculated within a grid cell corresponding to our CASTNET sites and compared with

344   observed $\Delta(^{17}O, HNO_3, pNO_3)$ at each site. The dominant annual pathway for nitrate formation in

345   the GEOS-Chem model ("base case") was N_2O_5 hydrolysis, which accounts for 50 % **(Figure 6)**,

346   followed by $NO_2 + OH$ (31 %) and $RONO_2$ hydrolysis (13 %) across all CASTNET sites. Nitrate

347   production via reaction of XNO_3 hydrolysis and $NO_3 + HC$ was small (< 1 %) at all sites. Strong

348   seasonality in nitrate production was observed as expected with high portions of N_2O_5 hydrolysis

349   in winter and $NO_2 + OH$ in summer **(Figure 6)**. Overall, the calculated $\Delta(^{17}O)$ showed a better

350   agreement with observed $\Delta(^{17}O)$ of pNO_3 ($y = 0.55 x + 12.62$ ($R^2 = 0.48$)) than $\Delta(^{17}O)$ of HNO_3 (y

351    $= 0.46 x + 10.68$ ($R^2 = 0.44$)) at all CASTNET sites (B = -2 % and 15 %, respectively) **(Figure 7)**.

352   The averaged residuals over the collection period for each site were 3.9 ‰, 2.8 ‰, and 5.6 ‰ for

353    $\Delta(^{17}O, HNO3)$, and 1.5 ‰, 1.7 ‰, and 6.1 ‰ for $\Delta(^{17}O, pNO_3)$ at ABT147, CTH110, and WST109,

354   respectively **(Figure 4)**. Calculated $\Delta(^{17}O)$ based on GEOS-Chem output reproduced the observed

355   temporal variations very well **(Figure 4 a and c)**. The GEOS-Chem model, however, does not

356   capture observed spatial $\Delta(^{17}O)$ variabilities. For instance, higher $\Delta(^{17}O)$ values (especially for

357   HNO_3) were observed at CTH110 compared to WST109; while no significant spatial $\Delta(^{17}O)$

358   difference was predicted from GEOS-Chem.

359

360   The GEOS-Chem model $\delta(^{18}O)$ was also calculated in the same manner as $\Delta(^{17}O)$ **(Figure 4 b and**

361   **d)**. Unlike calculated $\Delta(^{17}O)$, calculated $\delta(^{18}O)$ showed remarkably positive biases compared with

362   measured $\delta(^{18}O)$ of HNO_3 (B = 22 %) and pNO_3 (B = 21 %). The averaged residuals for $\delta(^{18}O,$

363    $HNO_3)$ at each site were 13.9 ‰, 12.9 ‰, and 19.6 ‰, and for $\delta(^{18}O, pNO_3)$ were 15.4 ‰, 14.2

364   ‰, and 18.2 ‰ at ABT147, CTH110, and WST109, respectively. Modeling the $\delta(^{18}O)$ values of

365   nitrate is more challenging than $\Delta(^{17}O)$ because not all oxidant $\delta(^{18}O)$ values have been directly

366   observed and fractionation factors associated with the O transfer into NO_y products is unknown.

367   Uncertainty in $\delta(^{18}O)$ values could be a major factor causing disagreement between observed and

368   calculated $\delta(^{18}O)$. Additionally, biases in the chemical mechanisms in GEOS-Chem could account

369   for the discrepancy.

370

371   Many studies have used $\Delta(^{17}O)$ to quantify and/or constrain modeled chemical mechanisms. Here,

372   GEOS-Chem production rates were optimized based on our observed $\Delta(^{17}O)$ to find the best linear

373   fit between observed and calculated $\Delta(^{17}O)$, and therefore constrain the predicted chemical

374   formation pathways. In other words, what relative production rates are predicted based on the

375   observations compared to the simulated values. GEOS-Chem was optimized based on $\Delta(^{17}O)$ of

376   HNO_3 and pNO_3 separately. Calculated $\Delta(^{17}O)$ from the base GEOS-Chem model was generally

377   1.15 times higher than observed $\Delta(^{17}O, HNO_3)$ and 0.98 times lower than $\Delta(^{17}O, pNO_3)$ across all

378   CASTNET sites. After optimization, the residuals between observed and calculated $\Delta(^{17}O)$

379   dramatically decreased (**Figure 4a and c)** and the linear relationships had slopes much closer to

380   the 1:1 line (i.e., from 0.46 to 1.03 for HNO_3 and from 0.55 to 0.78 for pNO_3**; Figure 7a and b**)

381   than the base GEOS-Chem model across the three CASTNET site (the relationships for each site

382   before and after optimization are shown in **Figure 7**). On a subannnual basis, the $\Delta(^{17}O)$

383   comparison for the cold season showed better improvement than the warm season, especially for

384    $\Delta(^{17}O, HNO_3)$.

385

386   Newly optimized nitrate production in GEOS-Chem was also applied to $\delta(^{18}O)$ calculation and

387   compared with previous results. As with $\Delta(^{17}O)$, a slope of the regression line between (optimized)

388   calculated and observed $\delta(^{18}O)$ became closer to 1 (i.e., from 0.30 to 0.74 for HNO_3 and from 0.39

389   to 0.49 for pNO_3; **Figure 7c and d**) and residuals improved at each site after the optimization

390   (**Figure 4b and d**). Overall, optimized GEOS-Chem $\delta(^{18}O)$ calculation shows better agreement

391   than the base GEOS-Chem model (B = -6 % for $\delta(^{18}O, HNO_3)$ and B = 13 % for $\delta(^{18}O, pNO_3)$),

392   but still has discrepancies, especially in the cold season (**Figure 4b and d**).

393

394   After optimization, the dominant pathway for nitrate formation in GEOS-Chem changed compared

395   to the base case. For $\Delta(^{17}O, pNO_3)$, NO_2 + OH (60 %) was the dominant pathway for nitrate

396   formation in the optimized GEOS-Chem calculation followed by N_2O_5 hydrolysis (31 %) and NO_3

Atmospheric
Chemistry
and Physics
Discussions
Open Access
EGU

397   hydrolysis (4 %) (**Figure 6**). At the same time, $\Delta(^{17}O, HNO_3)$ was almost entirely driven by NO_2

398   + OH reaction (98 %) in the optimized GEOS-Chem case. The optimized GEOS-Chem

399   calculations suggest that the fraction of nitrate produced by N_2O_5 hydrolysis was significantly

400   overestimated in GEOS-Chem base case since N_2O_5 hydrolysis contributes to high $\Delta(^{17}O)$ and

401   $\delta(^{18}O)$ values due to O_3 transfer. In the base case, N_2O_5 hydrolysis dominated nitrate production,

402   especially in the cold season with a fraction of over 68 % at all CASTNET sites (**Figure 6**). This

403   may also partly explain major nitrate concentration overestimates, particularly in the cold season.

404

405   **3.4 $\delta(^{18}O)$ optimization of atmospheric oxidants**

406   After optimization of relative nitrate production rates in GEOS-Chem based on $\Delta(^{17}O)$, we applied

407   the optimized chemical production to calculate $\delta(^{18}O)$, but still observed discrepancy between

408   observed and predicted $\delta(^{18}O)$. The discrepancy could be related to variable and somewhat

409   unconstrained $\delta(^{18}O)$ values of atmospheric oxidants important for nitrate formation. To test this,

410   the assumed (literature) $\delta(^{18}O)$ values of oxidants were optimized by selecting the best linear fit

411   between the observations and calculated $\delta(^{18}O, HNO_3$ and $pNO_3)$ (**Figure 8)**. After optimization

412   for $\delta(^{18}O)$ of oxidants, the discrepancy between observation and calculation was significantly

413   alleviated (**Figure 9**) with a decrease in B from 21 to 1 %. The optimization predicts $\delta(^{18}O)$ of H_2O

414   values similar to what was expected (-6.5 ‰ vs. -6.0 ‰), however significantly different values

415   were predicted for $\delta(^{18}O)$ of O_2, OH, and O_3 (**Table 2**). It is possible that this reflects isotope effects

416   associated with the incorporation of these oxidants during nitrate production, rather than further

417   issues with model chemistry since the relative production rates here are constrained based on

418   $\Delta(^{17}O)$. The $\delta(^{18}O, O_2)$ was a best fit with calculated $\delta(^{18}O)$ of nitrate values when assuming a

419   value of 11.1 ‰ (vs. the initial 23 ‰). Since atmospheric O_2 is incorporated into nitrate via NO

420   oxidation by HO_2 and RO_2 radicals, it was assumed that the $\delta(^{18}O)$ value of RO_2 and HO_2 is equal

421   to O_2 such that it does not consider any potential isotope effects associated with HO_2 and RO_2

422   formation and reaction with NO.

423

424   The observed $\delta(^{18}O)$ of O_3 and OH for the CASTNET samples were a best fit with calculated $\delta(^{18}O)$

425   when assuming values of 89.9 ‰ for $\delta(^{18}O, O_3)$ and 42.2 ‰ for $\delta(^{18}O, OH)$, respectively. In the

426   previous section, we noted that NO_2 + OH and N_2O_5 hydrolysis reactions were the dominant

427   pathways for nitrate formation, indicating that OH and O_3 play an important role in determining

428   the $\delta(^{18}O)$ value in nitrate. Indeed, optimizing $\delta(^{18}O)$ values to find the best agreement between

429   observation and calculation are largely dependent on $\delta(^{18}O)$ values of O_3 and OH (see also **Table**

430   **2**). The optimized $\delta(^{18}O, O_3^*)$ value (89.9 ‰) was lower than the average reported $\delta(^{18}O, O_3^*)$

431   ((126.3±12) ‰; Vicars and Savarino, 2014), though the $\delta(^{18}O, O_3)$ is known to vary with

432   temperature and pressure, and could also potentially be fractionated during reactions

433   (Brenninkmeijer et al., 2004). For example, Walters and Michalski, 2016 calculated an isotopic

434   enrichment factor near -20 ‰ associated with O_3 transfer in its reaction with NO, which would

435   lower the transferable $\delta(^{18}O)$ of O_3, consistent with our predictions. For $\delta(^{18}O, OH)$, the optimized

436   value dramatically increased compared to the initial assumed value (-43.0 ‰). The initial $\delta(^{18}O,$

437   OH) value is based on several assumptions that may not be correct regarding isotope exchange

438   with $H_2O(g)$. Additionally, Fang et al., 2021 suggested that $\delta(^{15}N)$ of nitrate is largely controlled

439   by an isotope effect in the NO_2 + OH pathway, and it could be conceivable that $\delta(^{18}O)$ may be

440   affected by a similar isotope effect as well. Overall, the optimization of $\delta(^{18}O, OH)$ is highly

441   dependent on the $\delta(^{18}O, O_3^*)$ (see **Table 2**), which makes sense given the proportional control of

442   the NO_2 + OH and N_2O_5 hydrolysis reaction. Despite the uncertainty in the transferrable $\delta(^{18}O)$

443   from major oxidants, the comparison between predicted and observed $\delta(^{18}O)$ and $\Delta(^{17}O)$ both

444   suggest a larger relative importance of NO_2 +OH chemistry than reflected in the model simulations.

445   We note here that this finding is also consistent with our study of $\delta(^{15}N, HNO_3)$ and $\delta(^{15}N, pNO_3)$,

446   as well from our companion study (acp-2022-621).

447

448   **4. Conclusions**

449

450   Using a combination of concentration and isotopic analyses, we evaluated atmospheric nitrate

451   formation pathways in the northeastern US in 2017–2018. The GEOS-Chem model showed large

452   positive biases for HNO_3 and pNO_3 concentrations, an important issue that is common in

453   atmospheric chemistry models. The observed oxygen isotopic compositions ($\Delta(^{17}O)$ and $\delta(^{18}O)$)

454   revealed that the model chemistry overpredicted heterogeneous hydrolysis of N_2O_5 for

455   atmospheric nitrate in the northeastern US A more important relative role of NO_2+OH chemistry

456   is also consistent with predicted seasonality in $\delta(^{15}N)$ of atmospheric nitrate in a companion study

457   (acp-2022-621). We also observed nitrate-phase differences in $\Delta(^{17}O)$ and $\delta(^{18}O)$, which are not

458   captured in current models. Further investigation of size-segregated nitrate chemistry is
459   recommended to improve model prediction of nitrate formation.

460

461   Traditionally, $\Delta(^{17}O)$ has been used to quantitatively assess nitrate production pathways. The use
462   of $\delta(^{18}O)$ as well can enhance our understanding of the oxidants contributing to nitrate formation,
463   particularly for distinguishing oxidants that have similar $\Delta(^{17}O)$ values (i.e., all are near 0 ‰ except
464   ozone). However, our study also observed a discrepancy between observed and calculated $\delta(^{18}O)$
465   values, even after accounting for an optimized chemical production based on $\Delta(^{17}O)$. The best
466   match of the observations suggests that the transferrable $\delta(^{18}O)$ values of oxidants may vary more
467   than is currently suggested in the literature. Better constraints, particularly on the isotopic
468   composition of OH and variability in $\delta(^{18}O, O_3)$ would add significant value to modeling and
469   interpretation of major oxidation chemistry in the atmosphere.

470

488

Atmospheric
Chemistry
and Physics
Discussions

Reference

Alexander, B., Hastings, M. G., Allman, D. J., Dachs, J., Thornton, J. A., and Kunasek, S. A.: Quantifying atmospheric nitrate formation pathways based on a global model of the oxygen isotopic composition (Δ^{17}O) of atmospheric nitrate, Atmospheric Chemistry and Physics, 9, 5043–5056, 2009.

Alexander, B., Sherwen, T., Holmes, C. D., Fisher, J. A., Chen, Q., Evans, M. J., and Kasibhatla, P.: Global inorganic nitrate production mechanisms: comparison of a global model with nitrate isotope observations, Atmospheric Chemistry and Physics, 20, 3859–3877, 2020.

Amos, H. M., Jacob, D. J., Holmes, C. D., Fisher, J. A., Wang, Q., Yantosca, R. M., Corbitt, E. S., Galarneau, E., Rutter, A. P., and Gustin, M. S.: Gas-particle partitioning of atmospheric Hg (II) and its effect on global mercury deposition, Atmospheric Chemistry and Physics, 12, 591–603, 2012.

Ashbaugh, L. L. and Eldred, R. A.: Loss of Particle Nitrate from Teflon Sampling Filters: Effects on Measured Gravimetric Mass in California and in the IMPROVE Network, Journal of the Air & Waste Management Association, 54, 93–104, https://doi.org/10.1080/10473289.2004.10470878, 2004.

Bates, K. H. and Jacob, D. J.: A new model mechanism for atmospheric oxidation of isoprene: global effects on oxidants, nitrogen oxides, organic products, and secondary organic aerosol, Atmospheric Chemistry and Physics, 19, 9613–9640, 2019.

Bekker, C., Walters, W.W., L. T. Murray, and Hastings, M. G.: Nitrate Chemistry in the Northeast US-Part I: Nitrogen Isotopic Seasonality Tracks with Nitrate Formation Chemistry,

Breider, T. J., Mickley, L. J., Jacob, D. J., Ge, C., Wang, J., Payer Sulprizio, M., Croft, B., Ridley, D. A., McConnell, J. R., and Sharma, S.: Multidecadal trends in aerosol radiative forcing over the Arctic: Contribution of changes in anthropogenic aerosol to Arctic warming since 1980, Journal of Geophysical Research: Atmospheres, 122, 3573–3594, 2017.

Brenninkmeijer, C. A., Janssen, C., Kaiser, J., Röckmann, T., Rhee, T. S., and Assonov, S. S.: Isotope effects in the chemistry of atmospheric trace compounds, Chemical Reviews, 103, 5125–5162, 2003.

Camargo, J. A. and Alonso, Á.: Ecological and toxicological effects of inorganic nitrogen pollution in aquatic ecosystems: a global assessment, Environment international, 32, 831–849, 2006.

Carter, T. (Tess) S., Joyce, E. E., and Hastings, M. G.: Quantifying Nitrate Formation Pathways in the Equatorial Pacific Atmosphere from the GEOTRACES Peru-Tahiti Transect, ACS Earth and Space Chemistry, 5, 2638–2651, 2021.

Casciotti, K. L., Sigman, D. M., Hastings, M. G., Böhlke, J. K., and Hilkert, A.: Measurement of the oxygen isotopic composition of nitrate in seawater and freshwater using the denitrifier method, Analytical chemistry, 74, 4905–4912, 2002.

CASTNET (Clean Air Status and Trends Network), Retrieved from United States Environmental Protection Agency, available at https://www.epa.gov/castnet, 2019

Atmospheric
Chemistry
and Physics
Discussions

529   Crutzen, P. J.: The role of NO and NO_2 in the chemistry of the troposphere and stratosphere,
530   Annual review of earth and planetary sciences, 7, 443–472, 1979.
531   Dubey, M. K., Mohrschladt, R., Donahue, N. M., and Anderson, J. G.: Isotope specific kinetics of
532   hydroxyl radical (OH) with water (H_2O): Testing models of reactivity and atmospheric
533   fractionation, The Journal of Physical Chemistry A, 101, 1494–1500, 1997.
534   Elliott, E. M., Kendall, C., Boyer, E. W., Burns, D. A., Lear, G. G., Golden, H. E., Harlin, K.,
535   Bytnerowicz, A., Butler, T. J., and Glatz, R.: Dual nitrate isotopes in dry deposition: Utility
536   for partitioning NO_x source contributions to landscape nitrogen deposition, Journal of
537   Geophysical Research: Biogeosciences, 114, 2009.
538   Fang, H., Walters, W. W., Mase, D., and Michalski, G.: i_NRACM: incorporating ^{15}N into the
539   Regional Atmospheric Chemistry Mechanism (RACM) for assessing the role photochemistry
540   plays in controlling the isotopic composition of NO_x, NO_y, and atmospheric nitrate,
541   Geoscientific Model Development, 14, 5001–5022, 2021.
542   Fountoukis, C. and Nenes, A.: ISORROPIA II: a computationally efficient thermodynamic
543   equilibrium model for K^+–Ca^{2+}–Mg^{2+}–NH_4^+–Na^+–SO_4^{2-}–NO_3^-–Cl^-–H_2O aerosols,
544   Atmospheric Chemistry and Physics, 7, 4639–4659, 2007.
545   Galloway, J. N., Dentener, F. J., Capone, D. G., Boyer, E. W., Howarth, R. W., Seitzinger, S. P.,
546   Asner, G. P., Cleveland, C. C., Green, P. A., and Holland, E. A.: Nitrogen cycles: past, present,
547   and future, Biogeochemistry, 70, 153–226, 2004.
548   Guenther, A. B., Jiang, X., Heald, C. L., Sakulyanontvittaya, T., Duhl, T. any, Emmons, L. K., and
549   Wang, X.: The Model of Emissions of Gases and Aerosols from Nature version 2.1 (MEGAN2.
550   1): an extended and updated framework for modeling biogenic emissions, Geoscientific Model
551   Development, 5, 1471–1492, 2012.
552   Hastings, M. G., Sigman, D. M., and Lipschultz, F.: Isotopic evidence for source changes of nitrate
553   in rain at Bermuda, Journal of Geophysical Research: Atmospheres, 108, 2003.
554   Heald, C. L., Collett Jr, J. L., Lee, T., Benedict, K. B., Schwandner, F. M., Li, Y., Clarisse, L.,
555   Hurtmans, D. R., Van Damme, M., and Clerbaux, C.: Atmospheric ammonia and particulate
556   inorganic nitrogen over the United States, Atmospheric Chemistry and Physics, 12, 10295–
557   10312, 2012.
558   Hering, S. and Cass, G.: The magnitude of bias in the measurement of $PM_{2.5}$ arising from
559   volatilization of particulate nitrate from Teflon filters, Journal of the Air & Waste Management
560   Association, 49, 725–733, 1999.
561   Hoesly, R. M., Smith, S. J., Feng, L., Klimont, Z., Janssens-Maenhout, G., Pitkanen, T., Seibert,
562   J. J., Vu, L., Andres, R. J., and Bolt, R. M.: Historical (1750–2014) anthropogenic emissions
563   of reactive gases and aerosols from the Community Emissions Data System (CEDS),
564   Geoscientific Model Development, 11, 369–408, 2018.
565   Holt, J., Selin, N. E., and Solomon, S.: Changes in inorganic fine particulate matter sensitivities to
566   precursors due to large-scale US emissions reductions, Environmental Science & Technology,
567   49, 4834–4841, 2015.
568   Hu, L., Millet, D. B., Baasandorj, M., Griffis, T. J., Turner, P., Helmig, D., Curtis, A. J., and
569   Hueber, J.: Isoprene emissions and impacts over an ecological transition region in the US

Upper Midwest inferred from tall tower measurements, Journal of Geophysical Research: Atmospheres, 120, 3553–3571, 2015.

Huang, J. and Jaeglé, L.: Wintertime enhancements of sea salt aerosol in polar regions consistent with a sea ice source from blowing snow, Atmospheric Chemistry and Physics, 17, 3699–3712, 2017.

Hudman, R. C., Moore, N. E., Martin, R. V., Russell, A. R., Mebust, A. K., Valin, L. C., and Cohen, R. C.: A mechanistic model of global soil nitric oxide emissions: implementation and space based-constraints., Atmospheric Chemistry & Physics Discussions, 12, 2012.

Jaeglé, L., Quinn, P. K., Bates, T. S., Alexander, B., and Lin, J.-T.: Global distribution of sea salt aerosols: new constraints from in situ and remote sensing observations, Atmospheric Chemistry and Physics, 11, 3137–3157, 2011.

Jaeglé, L., Shah, V., Thornton, J. A., Lopez-Hilfiker, F. D., Lee, B. H., McDuffie, E. E., Fibiger, D., Brown, S. S., Veres, P., and Sparks, T. L.: Nitrogen oxides emissions, chemistry, deposition, and export over the Northeast United States during the WINTER aircraft campaign, Journal of Geophysical Research: Atmospheres, 123, 12–368, 2018.

Kaiser, J., Hastings, M. G., Houlton, B. Z., Röckmann, T., and Sigman, D. M.: Triple oxygen isotope analysis of nitrate using the denitrifier method and thermal decomposition of N2O, Analytical Chemistry, 79, 599–607, 2007.

Kasibhatla, P., Sherwen, T., Evans, M. J., Carpenter, L. J., Reed, C., Alexander, B., Chen, Q., Sulprizio, M. P., Lee, J. D., and Read, K. A.: Global impact of nitrate photolysis in sea-salt aerosol on NO_x, OH, and O_3 in the marine boundary layer, Atmospheric Chemistry and Physics, 18, 11185–11203, 2018.

Kroopnick, P. and Craig, H.: Atmospheric oxygen: isotopic composition and solubility fractionation, Science, 175, 54–55, 1972.

Liu, H., Jacob, D. J., Bey, I., and Yantosca, R. M.: Constraints from ^{210}Pb and [7]Be on wet deposition and transport in a global three-dimensional chemical tracer model driven by assimilated meteorological fields, Journal of Geophysical Research: Atmospheres, 106, 12109–12128, 2001.

Luo, G., Yu, F., and Moch, J. M.: Further improvement of wet process treatments in GEOS-Chem v12.6.0: impact on global distributions of aerosols and aerosol precursors, Geoscientific Model Development, 13, 2879–2903, 2020.

Luo, G., Yu, F., and Schwab, J.: Revised treatment of wet scavenging processes dramatically improves GEOS-Chem 12.0.0 simulations of surface nitric acid, nitrate, and ammonium over the United States, Geoscientific Model Development, 12, 3439–3447, 2019.

McDuffie, E. E., Smith, S. J., O'Rourke, P., Tibrewal, K., Venkataraman, C., Marais, E. A., Zheng, B., Crippa, M., Brauer, M., and Martin, R. V.: A global anthropogenic emission inventory of atmospheric pollutants from sector- and fuel-specific sources (1970–2017): an application of the Community Emissions Data System (CEDS), Earth System Science Data, 12, 3413–3442, https://doi.org/10.5194/essd-12-3413-2020, 2020.

609 Michalski, G., Bhattacharya, S. K., and Mase, D. F.: Oxygen isotope dynamics of atmospheric
610   nitrate and its precursor molecules, in: Handbook of environmental isotope geochemistry,
611   Springer, 613–635, 2012.
612 Michalski, G., Scott, Z., Kabiling, M., and Thiemens, M. H.: First measurements and modeling of
613   Δ^{17}O in atmospheric nitrate, Geophysical Research Letters, 30, 2003.
614 Millet, D. B., Guenther, A., Siegel, D. A., Nelson, N. B., Singh, H. B., de Gouw, J. A., Warneke,
615   C., Williams, J., Eerdekens, G., Sinha, V., Karl, T., Flocke, F., Apel, E., Riemer, D. D., Palmer,
616   P. I., and Barkley, M.: Global atmospheric budget of acetaldehyde: 3-D model analysis and
617   constraints from in-situ and satellite observations, Atmospheric Chemistry and Physics, 10,
618   3405–3425, https://doi.org/10.5194/acp-10-3405-2010, 2010.
619 Morin, S., Sander, R., and Savarino, J.: Simulation of the diurnal variations of the oxygen isotope
620   anomaly (Δ^{17}O) of reactive atmospheric species, Atmospheric Chemistry and Physics, 11,
621   3653–3671, 2011.
622 Murray, L. T., Jacob, D. J., Logan, J. A., Hudman, R. C., and Koshak, W. J.: Optimized regional
623   and interannual variability of lightning in a global chemical transport model constrained by
624   LIS/OTD satellite data, Journal of Geophysical Research: Atmospheres, 117, 2012.
625 NEI (National Emissions Inventory): Retrieved from United States Environmental Protection
626   Agency, available at https://www.epa.gov/air-emissions-inventories/national-emissions-
627   inventory-nei, 2017.
628 Ridley, D. A., Heald, C. L., and Ford, B.: North African dust export and deposition: A satellite and
629   model perspective, Journal of Geophysical Research: Atmospheres, 117, 2012.
630 Savard, M. M., Cole, A. S., Vet, R., and Smirnoff, A.: The Δ^{17}O and δ^{18}O values of atmospheric
631   nitrates simultaneously collected downwind of anthropogenic sources–implications for
632   polluted air masses, Atmospheric Chemistry and Physics, 18, 10373–10389, 2018.
633 Savarino, J., Kaiser, J., Morin, S., Sigman, D. M., and Thiemens, M. H.: Nitrogen and oxygen
634   isotopic constraints on the origin of atmospheric nitrate in coastal Antarctica, Atmospheric
635   Chemistry and Physics, 7, 1925–1945, 2007.
636 Schlesinger, R. B.: The health impact of common inorganic components of fine particulate matter
637   (PM2. 5) in ambient air: a critical review, Inhalation toxicology, 19, 811–832, 2007.
638 Shah, V., Jaeglé, L., Thornton, J. A., Lopez-Hilfiker, F. D., Lee, B. H., Schroder, J. C.,
639   Campuzano-Jost, P., Jimenez, J. L., Guo, H., and Sullivan, A. P.: Chemical feedbacks weaken
640   the wintertime response of particulate sulfate and nitrate to emissions reductions over the
641   eastern United States, Proceedings of the National Academy of Sciences, 115, 8110–8115,
642   2018.
643 Sickles Ii, J. E. and Shadwick, D. S.: Air quality and atmospheric deposition in the eastern US: 20
644   years of change, Atmospheric Chemistry and Physics, 15, 173–197, 2015.
645 Sigman, D. M., Casciotti, K. L., Andreani, M., Barford, C., Galanter, M., and Böhlke, J. K.: A
646   bacterial method for the nitrogen isotopic analysis of nitrate in seawater and freshwater,
647   Analytical chemistry, 73, 4145–4153, 2001.

Atmospheric
Chemistry
and Physics
Discussions
Open Access
EGU

648 Tai, A. P., Mickley, L. J., and Jacob, D. J.: Correlations between fine particulate matter ($PM_{2.5}$)
649   and meteorological variables in the United States: Implications for the sensitivity of $PM_{2.5}$ to
650   climate change, Atmospheric environment, 44, 3976–3984, 2010.
651 Thiemens, M. H.: History and applications of mass-independent isotope effects, Annu. Rev. Earth
652   Planet. Sci., 34, 217–262, 2006.
653 US   EPA   (Environmental   Protection   Agency):   Our   nation's   air,   available   at
654   https://gispub.epa.gov/air/trendsreport/ 2017/, 2017.
655 van der Werf, G. R., Randerson, J. T., Giglio, L., van Leeuwen, T. T., Chen, Y., Rogers, B. M.,
656   Mu, M., van Marle, M. J. E., Morton, D. C., Collatz, G. J., Yokelson, R. J., and Kasibhatla, P.
657   S.: Global fire emissions estimates during 1997–2016, Earth System Science Data, 9, 697–720,
658   https://doi.org/10.5194/essd-9-697-2017, 2017.
659 Vicars, W. C. and Savarino, J.: Quantitative constraints on the ^{17}O-excess (Δ^{17}O) signature of
660   surface ozone: Ambient measurements from 50°N to 50°S using the nitrite-coated filter
661   technique, Geochimica et Cosmochimica Acta, 135, 270–287, 2014.
662 Vicars, W. C., Bhattacharya, S. K., Erbland, J., and Savarino, J.: Measurement of the ^{17}O-excess
663   (Δ^{17}O) of tropospheric ozone using a nitrite-coated filter, Rapid Communications in Mass
664   Spectrometry, 26, 1219–1231, 2012.
665 Vicars, W. C., Morin, S., Savarino, J., Wagner, N. L., Erbland, J., Vince, E., Martins, J. M. F.,
666   Lerner, B. M., Quinn, P. K., and Coffman, D. J.: Spatial and diurnal variability in reactive
667   nitrogen oxide chemistry as reflected in the isotopic composition of atmospheric nitrate:
668   Results from the CalNex 2010 field study, Journal of Geophysical Research: Atmospheres,
669   118, 10–567, 2013.
670 Walker, J. M., Philip, S., Martin, R. V., and Seinfeld, J. H.: Simulation of nitrate, sulfate, and
671   ammonium aerosols over the United States, Atmospheric Chemistry and Physics, 12, 11213–
672   11227, 2012.
673 Walters, W. W. and Michalski, G.: Theoretical calculation of oxygen equilibrium isotope
674   fractionation factors involving various NO_y molecules, OH, and H_2O and its implications for
675   isotope variations in atmospheric nitrate, Geochimica et Cosmochimica Acta, 191, 89–101,
676   2016.
677 Walters, W. W., Fang, H., and Michalski, G.: Summertime diurnal variations in the isotopic
678   composition of atmospheric nitrogen dioxide at a small midwestern United States city,
679   Atmospheric Environment, 179, 1–11, 2018.
680 Walters, W. W., Michalski, G., Böhlke, J. K., Alexander, B., Savarino, J., and Thiemens, M. H.:
681   Assessing the seasonal dynamics of nitrate and sulfate aerosols at the South Pole utilizing
682   stable isotopes, Journal of Geophysical Research: Atmospheres, 124, 8161–8177, 2019.
683 Wang, X., Jacob, D. J., Downs, W., Zhai, S., Zhu, L., Shah, V., Holmes, C. D., Sherwen, T.,
684   Alexander, B., and Evans, M. J.: Global tropospheric halogen (Cl, Br, I) chemistry and its
685   impact on oxidants, Atmospheric Chemistry and Physics, 21, 13973–13996, 2021.
686 Wesely, M. L. and Lesht, B. M.: Comparison of RADM dry deposition algorithms with a site-
687   specific method for inferring dry deposition, Water, Air, and Soil Pollution, 44, 273–293, 1989.

Atmospheric
Chemistry
and Physics
Discussions

688 Zhang, L., Jacob, D. J., Knipping, E. M., Kumar, N., Munger, J. W., Carouge, C. C., Van
689   Donkelaar, A., Wang, Y. X., and Chen, D.: Nitrogen deposition to the United States:
690   distribution, sources, and processes, Atmospheric Chemistry and Physics, 12, 4539–4554,
691   2012.
692
693
694
695
696
697
698
699
700
701
702
703
704
705
706
707
708
709
710
711
712
713
714
715
716
717
718
719
720
721
722
723
724
725
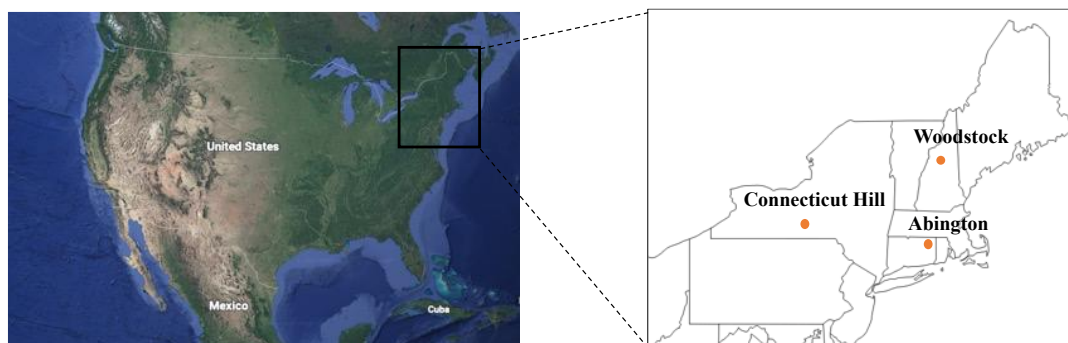
Figure 1. **Map of the United States (left) and selected CASTNET sites (right) for this study in the northeastern US. The image was created using © Google Earth (©2022 Google).**

(a) HNO$_3$
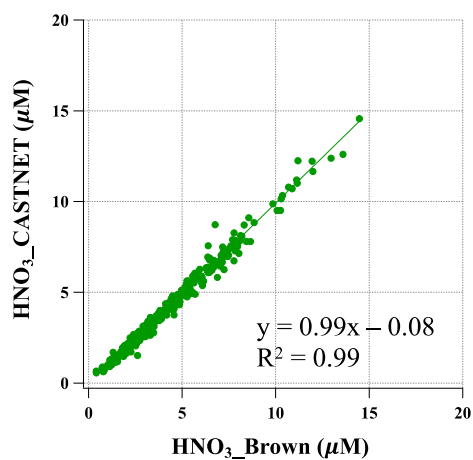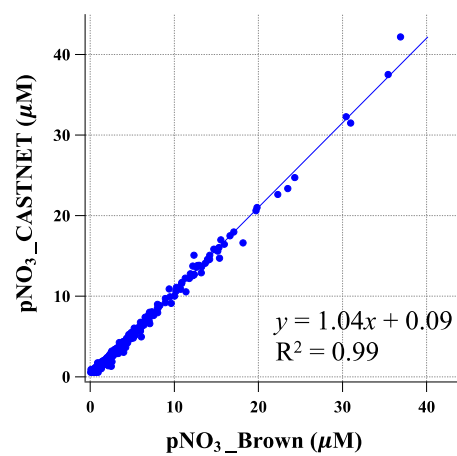
(b) pNO$_3$

Figure 2. Relationship of HNO$_3$ and pNO$_3$ filter extract concentrations reported by CASTNET and re-measured at Brown University.
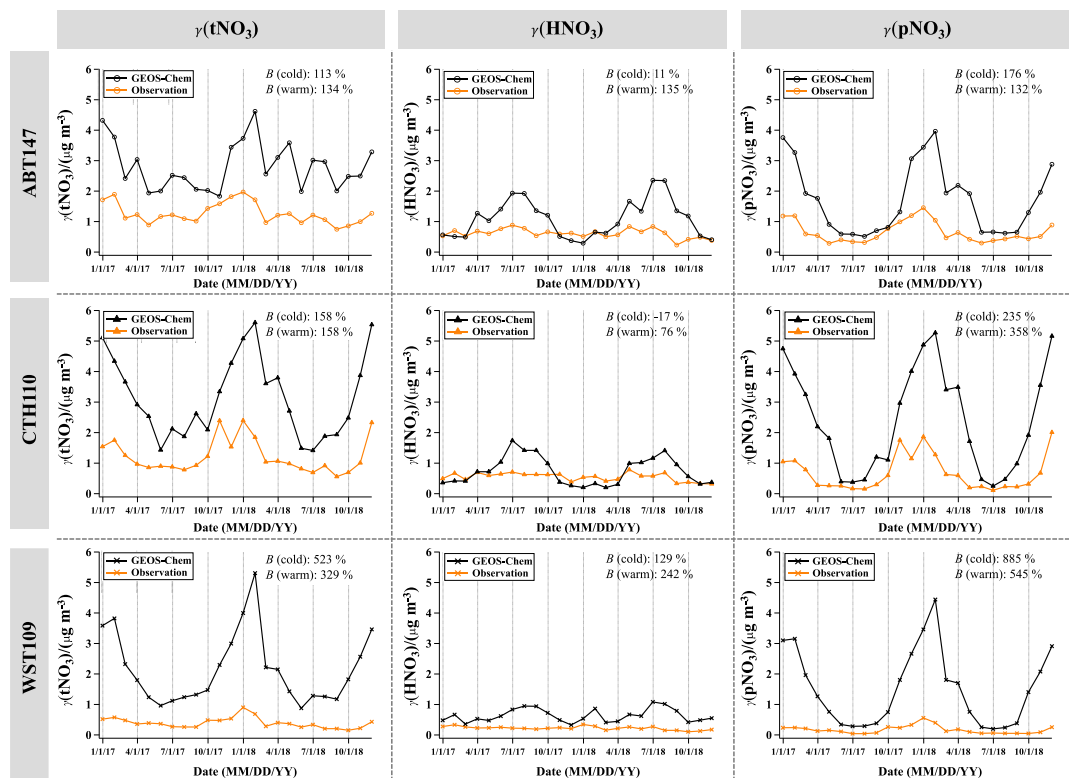
Figure 3. **Time series of monthly mean total nitrate, HNO₃, and pNO₃ concentrations (γ) observed and simulated at ABT147, CTH110, and WST109 CASTNET sites. *B* refers to the normalized mean bias for comparison of the model to observations (see section 2.3 in Methods).**

762

763

Figure 4. Time series of the monthly mean for observed and calculated $\Delta(^{17}O)$ and $\delta(^{18}O)$ for HNO$_3$ (a and b) and pNO$_3$ (c and d) over ABT147, CTH110, and WST109 CASTNET sites. Calculated $\delta(^{18}O)$ and $\Delta(^{17}O)$ using base (black) and optimized (grey) GEOS-Chem are shown in the plot together. Bars indicate the residuals between calculation and observation.
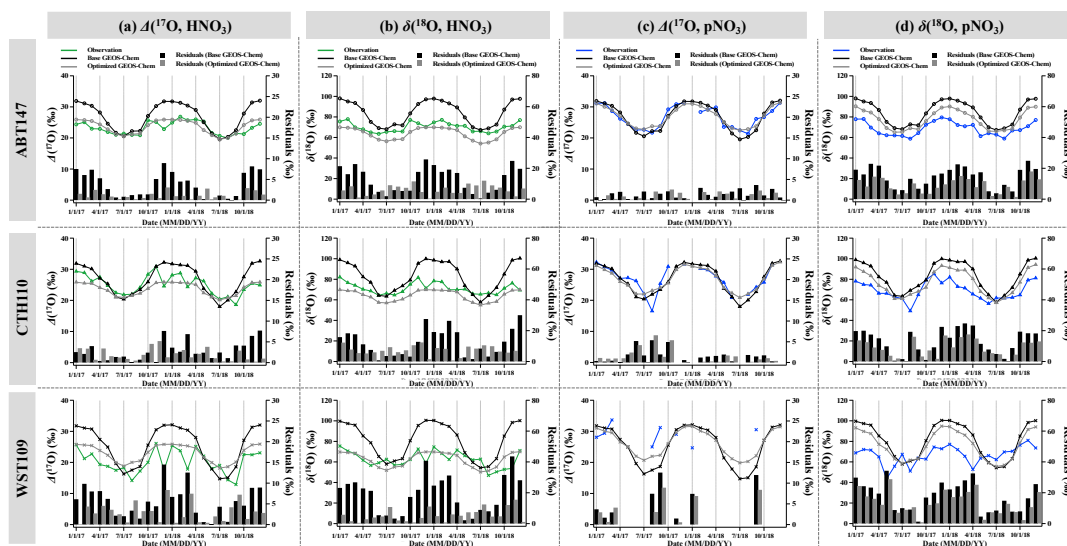
768

769

770

771

772

773
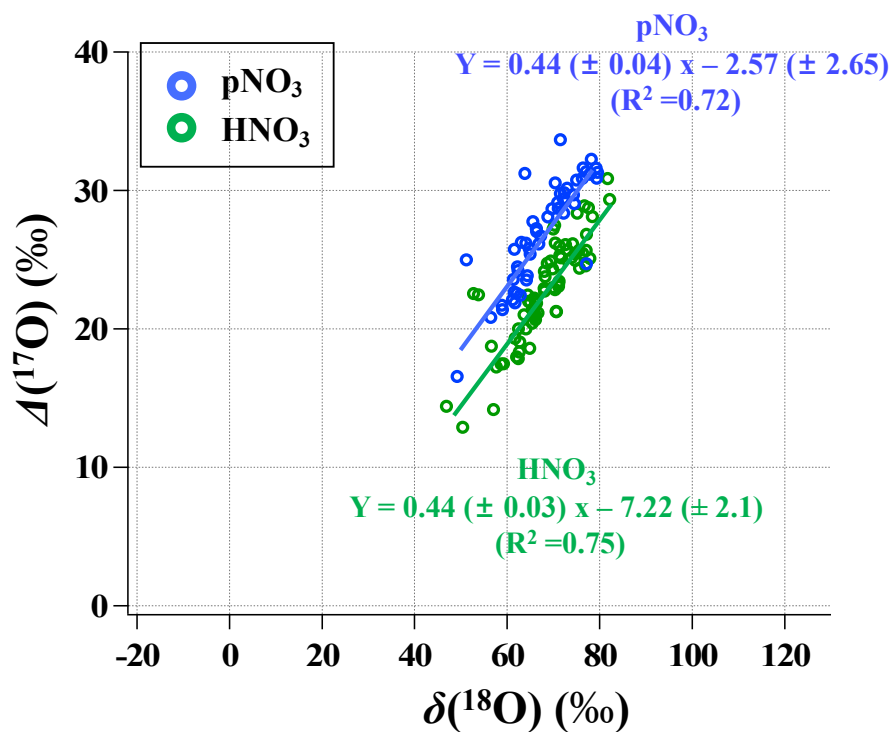
Figure 5. Relationship between the monthly mean ($\delta(^{18}O)$ and $\Delta(^{17}O)$) for observed HNO₃ (green) and pNO₃ (blue) across all CASTNET sites with correlation coefficient (R^2) and slope

774

775

776

777

778

779

780

781

782

783

784

785

786

787
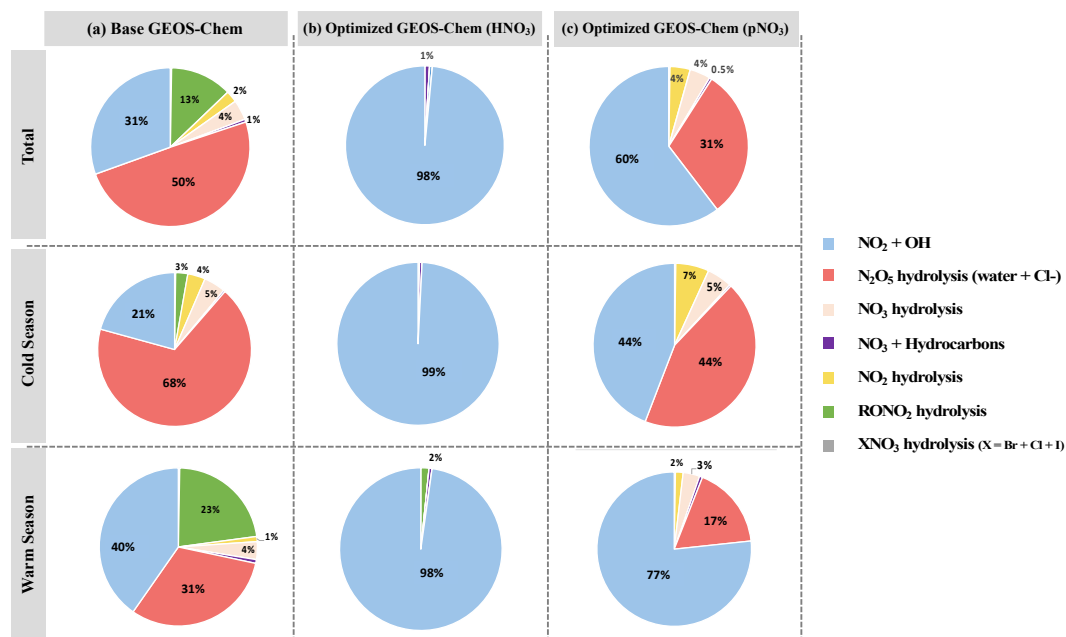
Figure 6. Relative proportions for major nitrate production pathways by season from (a) base GEOS-Chem output, (b) optimized GEOS-Chem for HNO₃ production, and (c) optimized GEOS-Chem for pNO₃ production based on comparison with observations across the three CASTNET sites.

792

793

794

795

796

797

798

799
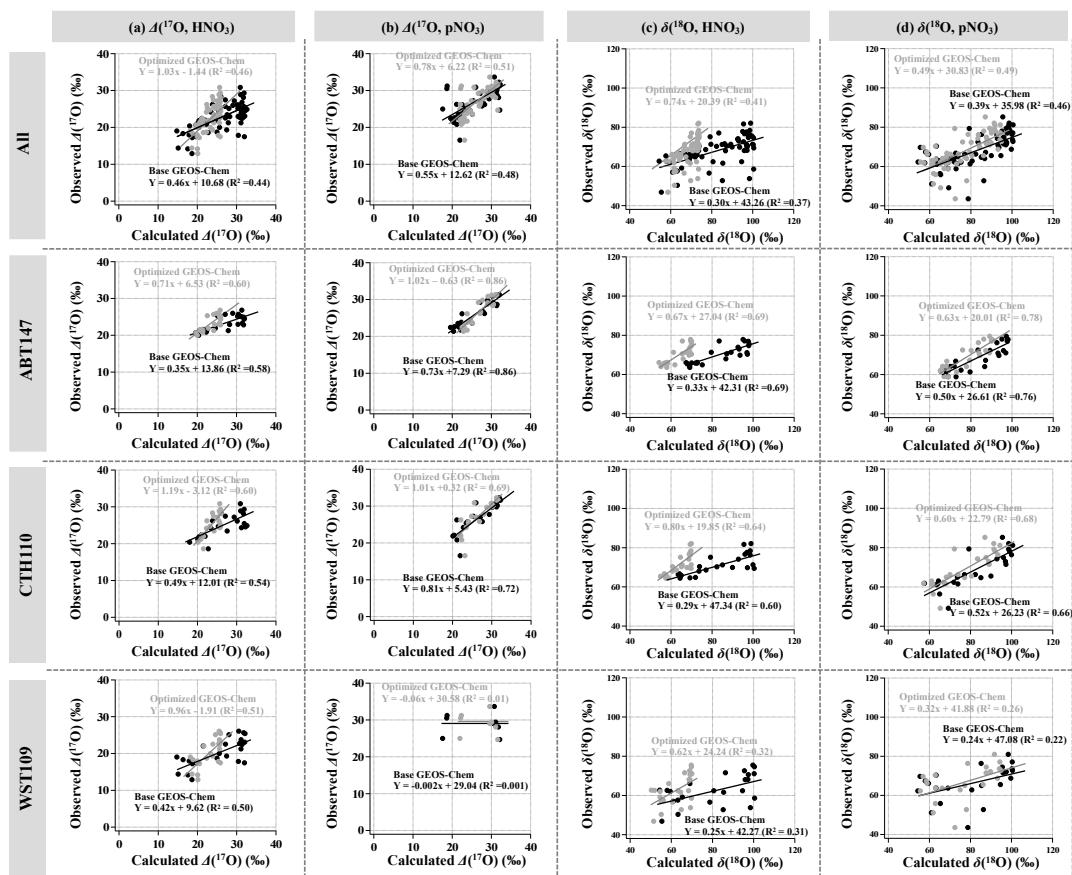
Figure 7. Correlation between observed and calculated Δ(^{17}O, HNO$_3$ and pNO$_3$) and δ(^{18}O, HNO$_3$ and pNO$_3$), respectively, using base GEOS-Chem (black) and optimized GEOS-Chem (grey) by each site.

803

804
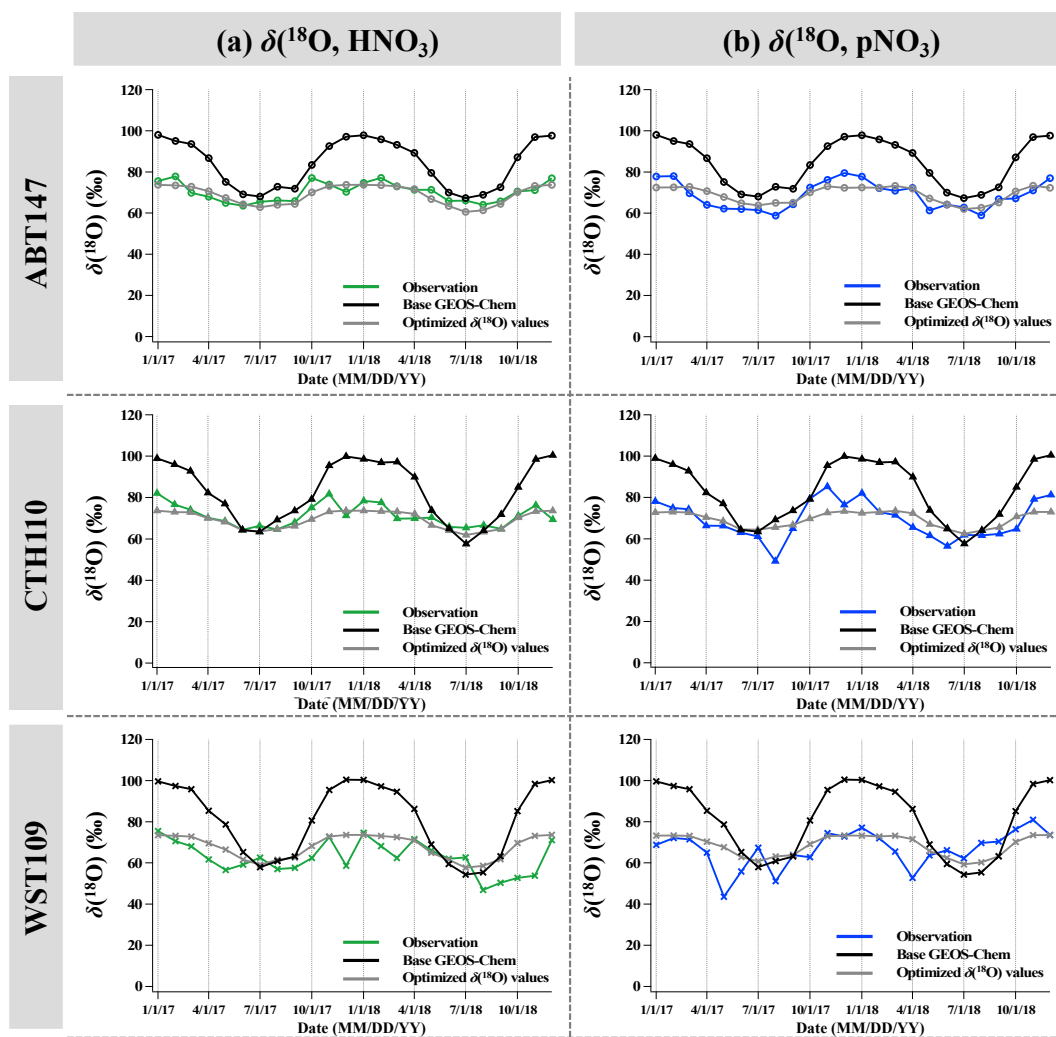
Figure 8. Time series of observed and calculated $\delta(^{18}O)$ for (a) HNO₃ and (b) pNO₃ for ABT147, CTH110, and WST109 sites. Calculated $\delta(^{18}O)$ using base GEOS-Chem (black) and using optimized $\delta(^{18}O)$ values (grey) are shown in the plot together.

805

806

807

808

809

810

811
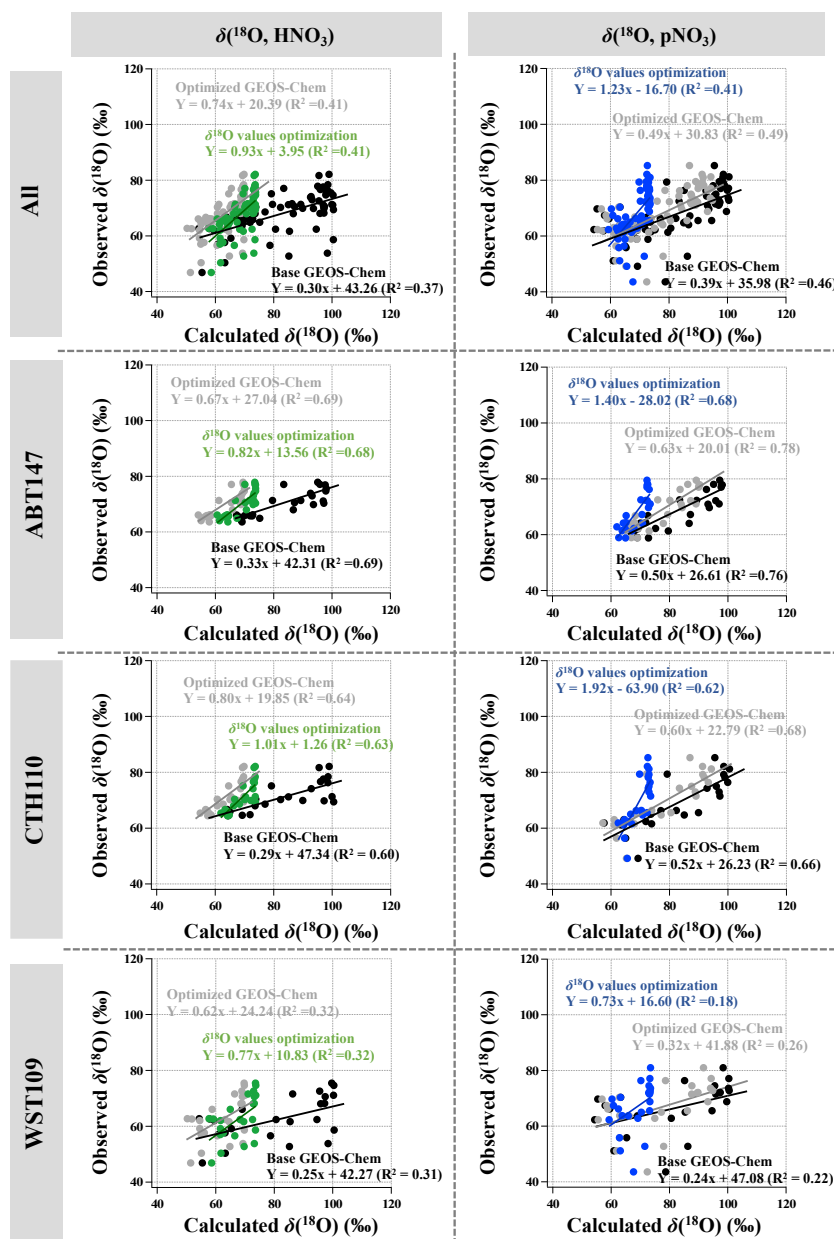
Figure 9. Correlation between observed and calculated $\delta(^{18}O$, HNO₃ and pNO₃) by each site.

Calculated $\delta(^{18}O)$ values using base GEOS-Chem, optimized GEOS-Chem, and optimized

$\delta(^{18}O)$ values indicated as black, grey, and green (for HNO₃) or blue (for pNO₃), respectively.

817 **Table 1.** Equations for $\delta(^{18}O)$ and $\Delta(^{17}O)$ calculations by different nitrate formation
818 **pathways.**

Gas-phase reactions	$\Delta(^{17}O, tNO_3)$	$\delta(^{18}O, tNO_3)$
$NO_2 + OH$	$\frac{2}{3}A\Delta(^{17}O, O_3^*)$	$\frac{2}{3}\delta(^{18}O, NO_2) + \frac{1}{3}\delta(^{18}O, OH)$
$NO_3 + Hydrocarbons$	$(\frac{2}{3}A+\frac{1}{3})\Delta(^{17}O, O_3^*)$	$\frac{2}{3}\delta(^{18}O, NO_2) + \frac{1}{3}\delta(^{18}O, O_3^*)$
Heterogeneous reactions		
N_2O_5 hydrolysis (water + Cl$^-$)	$(\frac{2}{3}A+\frac{1}{6})\Delta(^{17}O, O_3^*)$	$\frac{4}{6}\delta(^{18}O, NO_2) + \frac{1}{6}\delta(^{18}O, O_3^*) + \frac{1}{6}\delta(^{18}O, H_2O)$
NO_3 hydrolysis	$(\frac{2}{3}A+\frac{1}{3})\Delta(^{17}O, O_3^*)$	$\frac{2}{3}\delta(^{18}O, NO_2) + \frac{1}{3}\delta(^{18}O, O_3^*)$
NO_2 hydrolysis	$(\frac{2}{3}A+\frac{1}{3})\Delta(^{17}O, O_3^*)$	$\frac{2}{3}\delta(^{18}O, NO_2) + \frac{1}{3}\delta(^{18}O, H_2O)$
$RONO_2$ hydrolysis	$\frac{1}{3}A\,\Delta(^{17}O, O_3^*)$	$\frac{2}{3}\delta(^{18}O, NO_2) + \frac{1}{3}\delta(^{18}O, NO_2)$
XNO_3 hydrolysis (X = Br + Cl + I)	$(\frac{2}{3}A+\frac{1}{3})\Delta(^{17}O, O_3^*)$	$\frac{2}{3}\delta(^{18}O, NO_2) + \frac{1}{3}\delta(^{18}O, O_3^*)$

819
820
821
822
823
824
825
826
827
828
829
830
831
832
833
834
835
836
837
838

839 **Table 2. $\delta(^{18}O)$ values for each oxidant before and after optimization based on different**

840 **scenarios**

Atmospheric Oxidants	Assumed $\delta(^{18}O)$ (‰)	Optimized $\delta(^{18}O)$ (‰)			
		Non-fixed	Fixed O_3^*	Fixed O_3^* and H_2O	Fixed O_3^*, H_2O, and O_2
O_3^*	126.3	89.9	-	-	-
H_2O	-6.0	-6.5	-180.7	-	-
$O_2/RO_2/HO_2$	23.0	11.1	40.9	44.4	-
OH	-43.0	42.2	-31.3	-39.4	-36

841

842

843

844